Nuclear Inst. and Methods in Physics Research, A 1055 (2023) 168522

Contents lists available at ScienceDirect

Nuclear Inst. and Methods in Physics Research, A

journal homepage: www.elsevier.com/locate/nima

Full Length Article

Timing performance and gain degradation after irradiation with protons and neutrons of Low Gain Avalanche Diodes based on a shallow and broad multiplication layer in a float-zone 35 μm and 50 μm thick silicon substrate

E. Currás [a,*], A. Doblas [c], M. Fernández [a,b], D. Flores [c], J. González [b], S. Hidalgo [c], R. Jaramillo [b], M. Moll [a], E. Navarrete [b], G. Pellegrini [c], I. Vila [b]

[a] CERN, Organisation européenne pour la recherche nucléaire, CH-1211 Geneve 23, Switzerland
[b] Instituto de Física de Cantabria, IFCA (CSIC-UC), Avda. los Castros s/n, E-39005 Santander, Spain
[c] Instituto de Microelectrónica de Barcelona (IMB-CNM-CSIC), E-08193 Bellaterra (Barcelona), Spain

ARTICLE INFO

Keywords:
LGAD
Timing detector
Gain
Jitter
Slew rate
Shallow junction

ABSTRACT

The high-luminosity upgrade of the ATLAS and CMS experiments includes dedicated sub-detectors to perform the time-stamping of minimum ionizing particles (MIPs). These detectors will be exposed up to fluences in the range of 1.5–2.5 × 10^{15} n_{eq}/cm^2 and require a time resolution per detecting layer of 30 ps, for non-irradiated sensors, to 50–70 ps (depending on the exposed fluences) for sensors at the end of their lifetime. To cope with these requirements, the low-gain avalanche diode (LGAD) has been chosen as the baseline detection technology. In this article, an in-depth radiation tolerance study on LGADs manufactured at IMB-CNM using a so-called *shallow junction* is presented. Proton irradiation at CERN-PS up to fluences of 3 × 10^{15} n_{eq}/cm^2 and neutron irradiation at JSI-Ljubljana up to 2.5 × 10^{15} n_{eq}/cm^2 were performed. Two different active thicknesses were studied: 35 μm and 50 μm. Gain degradation, operation stability, and timing performance were evaluated.

1. Introduction

The high-luminosity upgrade of the Large Hadron Collider (HL-LHC) is foreseen to start at the beginning of 2029 delivering an integrated luminosity up to 4000 fb^{-1} during its 10 years of operation. The HL-LHC will operate at a stable luminosity of 5.0 × 10^{34} cm^{-2} s^{-1}, with an ultimate scenario of 7.5 × 10^{34} cm^{-2} s^{-1} [1]. The superposition of multiple proton–proton collisions per bunch crossing, referred to as *pileup*, will be one of the main challenges of the HL-LHC. The multiple-collision region will spread over about 50 mm in RMS along the beam axis with an average of 1.6 collisions/mm for an average of 200 pp interactions per bunch crossing. Under these conditions, a major challenge is to disentangle the multiple collisions per bunch crossing to correctly associate the reconstructed track to its primary production vertex. It is possible to determine if two tracks are coming from a given interaction by comparing the track time with the primary vertex time. With this purpose, MIP timing sub-detectors are proposed [2,3]. Providing a time resolution of 30 ps per track, these detectors will be able to disentangle the high number of pileup events and improve the performance of the ATLAS and CMS detectors.

The MIP timing sub-detector sensors will be made of Low Gain Avalanche Diodes (LGAD) [4–6]. LGADs are semiconductor detectors with signal amplification, that are implemented as n^{++}–p^{+}–p avalanche diodes. The highly-doped p^{+} layer is added to create a very high electric field region. This electric field generates the avalanche multiplication of the primary electrons, creating additional electron–hole pairs. The schematic cross-section of a standard pad-like LGAD is shown in Fig. 1. The LGAD structure is designed to exhibit a moderate gain and operate over a wide range of reverse bias voltages before breakdown. Moreover, microstrip and pixel detector layouts can be also obtained with the LGAD approach with a relatively high Signal-to-Noise Ratio (SNR) value, in comparison with a standard PIN-like detector. Currently, there are several approaches under study using the LGAD technology aiming to improve the spatial resolution to cope with the high occupancy in future tracking experiments [7]. Therefore, precise measurements of the position and time of arrival of the incident particles can be also achieved with LGADs.

As previously stated, for the HL-LHC, the ATLAS and CMS experiments will include dedicated sub-detectors to perform timing measurements of minimum ionizing particles (MIPs). The ATLAS High Granularity Timing Detector (HGTD) will provide a timing resolution of 30 ps. This sub-detector is proposed to be built using LGADs with a pixel size of 1.3 × 1.3 mm^2. The same timing performance and pixel geometry is foreseen for the CMS Endcap Timing layer (ETL). These

* Corresponding author.
E-mail address: ecurrasr@cern.ch (E. Currás).

https://doi.org/10.1016/j.nima.2023.168522
Received 23 December 2022; Received in revised form 13 June 2023; Accepted 1 July 2023
Available online 6 July 2023

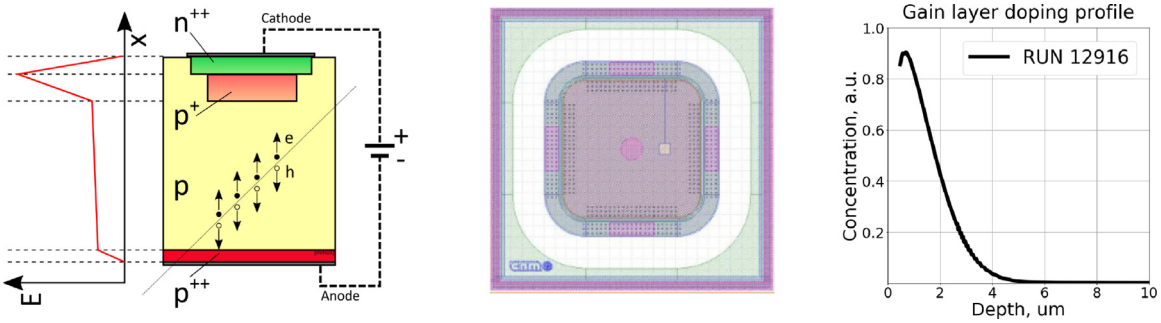

Fig. 1. In the left: schematic view of the Low Gain Avalanche Diode (LGAD) [8]. In the middle: top view of the samples' layout used for this study. They are pad-like LGADs with an active area of 1.3×1.3 mm^2 and two different active thicknesses: 35 and 50 μm. In the right: gain layer doping profile extracted from the electrical characterization.

Table 1
Table summarizing all the proton-irradiated LGADs used for this study. In total, 20 LGADs plus 4 PINs coming from wafer 5 and wafer 11 from the CNM run 11748 were available.

Wafer 5 (35 μm)	Wafer 11 (50 μm)	Fluence (p^+/cm^2)	Fluence (n_{eq}/cm^2)
$2 \times LGADs$	$2 \times LGADs$	1×10^{14}	6×10^{13}
$2 \times LGADs$	$2 \times LGADs$	1.7×10^{14}	1×10^{14}
$2 \times LGADs$	$2 \times LGADs$	5×10^{14}	3×10^{14}
$2 \times LGADs$	$2 \times LGADs$	1.7×10^{15}	1×10^{15}
$2 \times LGADs$	$2 \times LGADs$	5×10^{15}	3×10^{15}

detectors will be exposed to radiation levels up to $2.5 \times 10^{15}\, n_{eq}/cm^2$ (ATLAS HGTD) and $1.5 \times 10^{15}\, n_{eq}/cm^2$ (CMS Endcap).

2. Samples description

The LGADs used for this study were produced by IMB-CNM.[1] The production runs were:

- The run number 11748 and within this run, LGADs and PINs coming from wafer 5 (W5) and wafer 11 (W11) were studied. The only difference between these two wafers was the active thickness, 35 μm for W5 and 50 μm for W11, both are Silicon-on-Silicon wafers with a 300 μm thick, low resistivity, support wafer, directly bonded to the high-resistivity *active* wafer.
- The run number 12916 and within this run, LGADs and PINs coming from wafers 2 (W2) and 4 (W4) were studied. The active thickness was 50 μm and both are Silicon-on-Silicon wafers with a 300 μm thick, low resistivity, support wafer, directly bonded to the high-resistivity *active* wafer.

For the study, 26 pad-like LGADs plus 18 PINs were used. The total area of all the devices was 2.6×2.6 mm^2 with an active area of 1.3×1.3 mm^2, and one guard ring structure was included. A small opening on the metallization of 100×100 μm^2, to allow light illumination, was included. Also, the samples had a Junction Termination Extension (JTE) with the objective to increase gain homogeneity and to have higher voltage stability. In Fig. 1 middle plot, a top view drawing of these sensors, where it is possible to observe all described features, is shown. The implantation dose to create the gain layer (GL) was in the order of 1.8×10^{13} atoms/cm^2 with shallow junction implantation. In Fig. 1 (right plot), the doping profile of the GL extracted from the capacitance vs voltage curves is shown.

The only difference in the design of samples from run 12916 compared with samples from run 11748 was a modification in the JTE structure that corrected a design problem found in run 11748 and will be explained in the next section of this paper. Due to this modification of the JTE structure, the LGADs from run 12916 show a higher gain than the LGADs from run 11748.

[1] Centro Nacional de Microelectrónica. Instituto de Microelectrónica de Barcelona, IMB-CNM CSIC

Table 2
Table summarizing all the neutron-irradiated LGADs used for this study. In total, there were available 16 LGADs plus 8 PINs coming from wafer 2 and wafer 4 from the CNM run 12916.

Wafer 2 (50 μm)	Wafer 4 (50 μm)	Fluence (n_{eq}/cm^2)
$2 \times LGADs$	$2 \times LGADs$	4.0×10^{14}
$2 \times LGADs$	$2 \times LGADs$	8.0×10^{14}
$2 \times LGADs$	$2 \times LGADs$	1.5×10^{15}
$2 \times LGADs$	$2 \times LGADs$	2.5×10^{15}

The samples from run 11478 were irradiated at the CERN-PS with 24 GeV/c protons [9] at 5 different fluences. In Table 1 a summary of all LGADs available and all the irradiation fluences is shown. The applied hardness factor for conversion into 1 MeV neutron equivalent damage was 0.6 [10], and the fluences were achieved within an error of 7%. An annealing of 10 min at 60 °C was performed on all the samples right after irradiation. Two PINs diodes and two LGADs were kept unirradiated for reference.

The samples from run 12916 were irradiated at the Jožef Stefan Institute (JSI) in Ljubjana [11] with neutrons at 4 different fluences. In Table 2 a summary of all LGADs available and all the irradiation fluences is shown. The fluences were achieved within an error of 10%. An annealing of 80 min at 60 °C was performed on all samples right after irradiation. Two PINs diodes and two LGADs were not irradiated and were kept for reference.

3. Electrical characterization

The electrical characterization was performed at the SSD labs at CERN and at IFCA in Santander (Spain). A probe station to measure the bare samples before and after irradiation was used. The samples were placed directly on a chuck that can be temperature controlled. The leakage current and the capacitance as a function of the reverse bias voltage were measured. During the electrical characterization, the guard ring was always grounded.

3.1. Current vs voltage measurements

The pad current as a function of the reverse bias was measured before irradiation for all the devices. These measurements were done at 20 °C and the results are shown in Fig. 2. On the left-hand plot, a

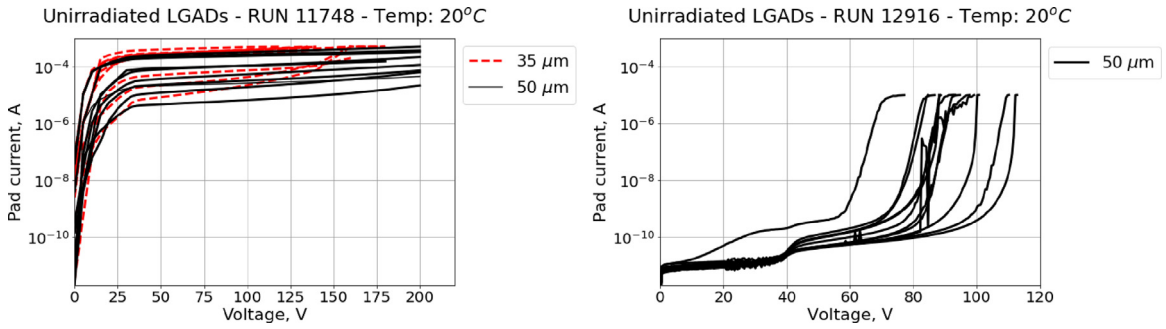

Fig. 2. On the left side plot, pad currents from the run 11748 LGADs measured before irradiation are shown. A very high pad current with a high dispersion among different sensors was observed. On the right side plot, pad currents from the run 12916 LGADs measured before irradiation are given. These samples show a much smaller pad current with a clear indication of the breakdown voltage, which varies from 65 V to 115 V.

very high leakage current with a high dispersion between the different samples in the LGADs from run 11748, for both wafers, is observed. In this plot, the results for the PINs samples were not included, but they presented a typical pad current in the range of the pA as it was expected. It was observed that this high leakage current, present in all the LGADs, was not coming from the bulk because it was not observed in the PIN diodes and it was not scaling with temperature as it would be expected for a generation current from crystal defects. In fact, the measured current was increasing when the temperature was decreased. The source of this high leakage current will be discussed in the next section and it was resolved in run 12916. On the right-hand plot, the results for the LGADs from run 12916 are shown, PINs are not shown in this plot. Very low pad current is reported for all the LGADs with low dispersion between samples. The depletion voltage of the gain layer (V_{GL}) around 40 V is visible as well as the breakdown voltages (V_{BD}). The V_{GL} is very homogeneous but the V_{BD} presents an important dispersion between samples before irradiation, that ranges between 65 V and 115 V at 20° C.

After irradiation, and after the mentioned annealing, the pad current as a function of the reverse bias was measured again at a temperature of −20 °C. The results for run 11748 are shown in Fig. 3 on the left-hand side plot. It is remarked that at low fluences the measured current is very similar before and after irradiation. But at higher fluences, it is observed that the leakage current is decreasing with fluence. The LGADs irradiated at 3×10^{15} n_{eq}/cm^2 are the ones with the lowest leakage current. Thus, the mechanism that was causing this anomalous high leakage current has been minimized by the irradiation. In this aspect, no differences were observed after irradiation between the two wafers. It was not possible to accurately extract the breakdown voltage from the current measurements as a result of the high leakage current that was dominating the total current. Also, the evaluation of the bulk current arising from radiation damage was not possible either for the same issue. The results for run 12916 are shown on the right-hand side plot of Fig. 3. In this case, the behavior of the pad current follows the expectations after the irradiation. An increase of the pad current and the V_{BD} with the irradiation fluence is observed. The increase of the V_{BD} with the irradiation fluence is an indication of the degradation of the gain layer with the irradiation fluence.

3.2. Capacitance vs voltage measurements

The capacitance curve as a function of the reverse bias voltage was measured before and after irradiation for all the samples. Before irradiation, the measurements were done at 20 °C, with the guard ring grounded and the LCR meter frequency set to 1 kHz. The circuit model used to determine the capacitance was a parallel RC circuit. The results can be seen in Fig. 4 on the left-hand side plot for run 11748 and on the right-hand side plot for run 12916. The reference PINs samples are not plotted. It can be observed that the capacitance starts decreasing smoothly while the gain layer is being depleted. The gain layer is finally depleted at around 35–40 V. Then, a more noticeable drop in the capacitance is observed which indicates the depletion of the bulk. The final end-capacitance (C_{end}) is reached above ∼40 V. For all the samples the capacitance curves look very similar, where the only difference appears in the value of the C_{end}. For the 35 μm LGADs the C_{end} is about 6.5 pF while for the 50 μm LGADs the C_{end} is about 4.0 pF. In both cases, it is in agreement with the value expected according to the dimensions of the samples. For the PIN diodes, the full depletion is reached below 5 V.

After irradiation and after the mentioned annealing, the capacitance was measured again at a temperature close to room temperature and with a low frequency set in the LCR meter. This was done to extract with more precision the GL doping profile and the V_{GL} after irradiation [12,13]. The guard ring was always grounded. In Fig. 5 on the left-hand side plot, the capacitance curves for run 11748 after irradiation for some of the LGADs are shown. For clarity, LGADs that exhibited noisy capacitance curves were excluded from this plot. The C_{end} remains the same as before irradiation, but an evident increase of the V_{GL} up to a fluence of 3×10^{14} n_{eq}/cm^2 is observed. This feature is not fully understood yet but has been observed before after proton irradiation of LGADs with thick bulk layers [14]. Thus, for these samples, the acceptor removal effect cannot be analyzed from the extracted V_{GL} values as the tendency should be the opposite one: a decrease of the V_{GL} with fluence. Nevertheless, these contradictory results could be due to the presence of a double-junction mechanism. This effect would be more in the line with the observed results, but the analysis of the capacitance curve is complicated because of the high leakage current in these samples, which could play an important role. This has to be better understood. In Fig. 5 on the right-hand side plot, the capacitance curves for run 12916 after irradiation are shown. In this case, a clear decrease of the V_{GL} with fluence is observed, as it is expected from the acceptor removal effect [15].

4. Leakage current analysis

We have analyzed the high leakage current observed during the I-V measurements on the LGADs from run 11748 by means of 2D numerical simulations of the peripheral area, assuming that this problem could be linked to a JTE structure design modification for this run that was targeting an increase in high voltage stability. The 2D simulation results indeed demonstrated that if the overlap between the N^+ and JTE diffusion on the multiplication layer is reduced, the doping in that area might not be compensated, inducing a parallel p-type resistor that connects the anode with the cathode. In this situation, the leakage current increases dramatically as we can see in Fig. 6.

We used thermographic measurements to confirm this hypothesis. The measurements carried out at CNM show that the source of this high leakage current is located at the periphery of the samples, just where the JTE is placed. In Fig. 7, we can see several points of high current generation located in the periphery of the LGAD structure, at

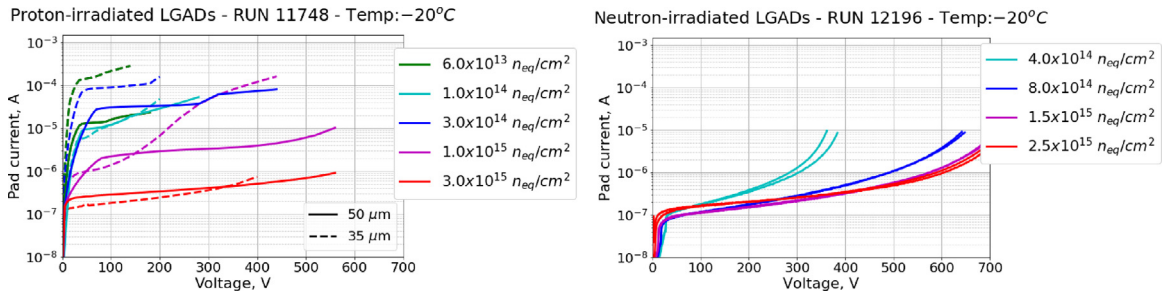

Fig. 3. On the left side plot, pad currents from the run 11748 LGADs measured after proton irradiation are shown. The pad current decreases with fluence indicating that the current generation mechanism driving the high current is being suppressed by the irradiation. On the right side plot, pad currents from the run 12916 LGADs measured after neutron irradiation are shown. A clear increase in the breakdown voltage with fluence is visible.

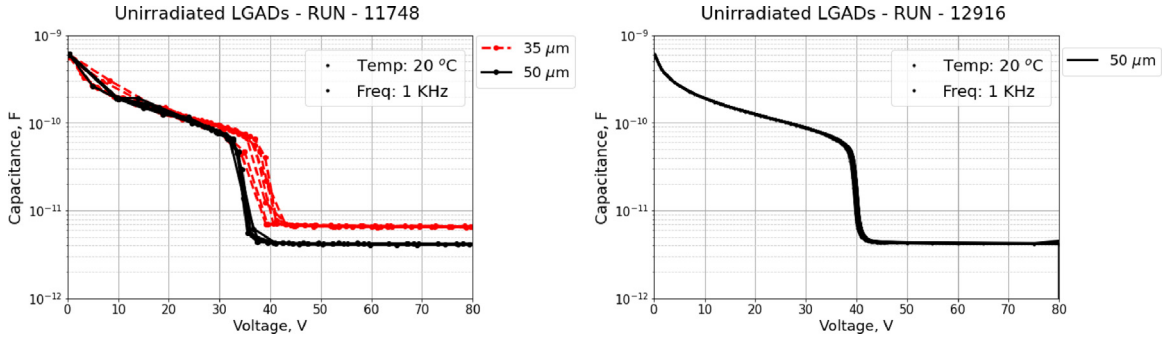

Fig. 4. On the left side plot, capacitance vs. voltage from the run 11748 LGADs measured before irradiation are given. The V_{GL} is observed around 40 V. C_{end} is in agreement with expected values according to the dimensions of the device. For W5 is ∼6.5 pF and for W11 is ∼4.0 pF. On the right side plot, 50 μm LGADs capacitance from run 12916 measured before irradiation. The C_{end} does not change, and the V_{GL} is at 40 V.

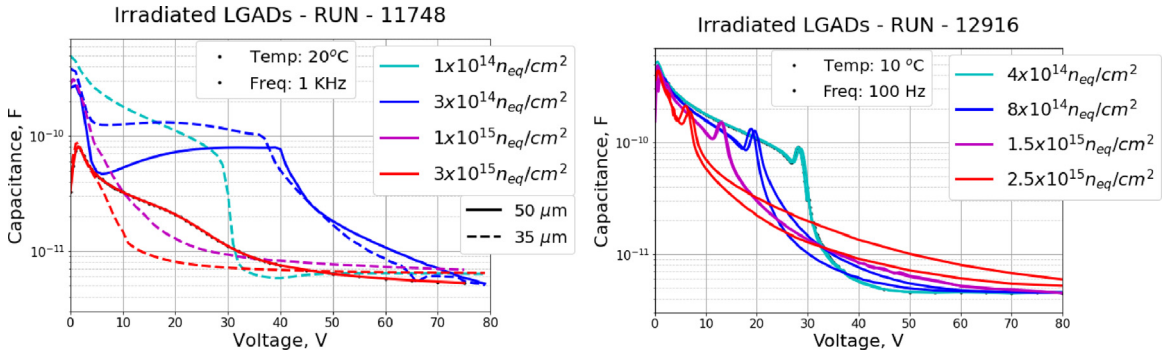

Fig. 5. On the left side plot, LGADs capacitance vs voltage curves from run 11748 measured after irradiation are shown. The C_{end} is the same as before irradiation, but the V_{GL} is increasing with increasing fluence. On the right side plot, LGADs capacitances from run 12916 measured after irradiation are shown. In this case, a clear reduction of the V_{GL} with fluence is observed.

low voltage (left image), increasing its number and intensity as the voltage applied to the LGAD increases (right image).

In order to overcome this problem, we redesigned the N^+ layer to overlap the JTE diffusion. In this second design, the overlap between the N^+ layer and the JTE structure was increased. LGADs from run 12916, fabricated with this new design, show low leakage currents, as expected.

5. Radiation-induced acceptor removal

Due to the previously mentioned problem in run 11748, the acceptor removal effect could only be studied in the samples from run 12916. The deactivation of the Boron (B) implanted in the GL with fluence, is linked with the reduction of the voltage needed to deplete the GL. If there is less active B inside the GL, the reverse bias voltage needed to fully deplete the GL is lower. Following this assumption, it is possible to extract the V_{GL}, and in consequence the amount of active B remaining inside the GL, using different techniques. In this paper, we are going to explore three different methods to evaluate the amount of active B remaining. The first two methods use V_{GL} as an approximation for the active B concentration using the data from the electrical characterization, and the third method uses a measurement of the complete doping profile extracted also from the electrical characterization. The initial acceptor removal is exponentially dependent on fluence, and it is defined in Eq. (1), where c is the removal constant, $N_{x,0}$ initial doping concentration, and $V_{GL,0}$ the initial depletion voltage of the GL [15].

$$N_x = N_{x,0}\ exp(-c\,\Phi_{eq}) \ \Rightarrow\ V_{GL} \approx V_{GL,0}\ exp(-c\,\Phi_{eq}) \tag{1}$$

In Fig. 8 the three different methods are depicted. On the left plot is shown how the V_{GL} is extracted from the pad current. When the GL is fully depleted, there is a very quick increase in the pad current due to the sudden contribution of the bulk current. This can be easily seen and computed using the derivative of the pad current, using the following formula: $dI_p/dV \times (V/I_p)$, as shown in Fig. 8 left. From the

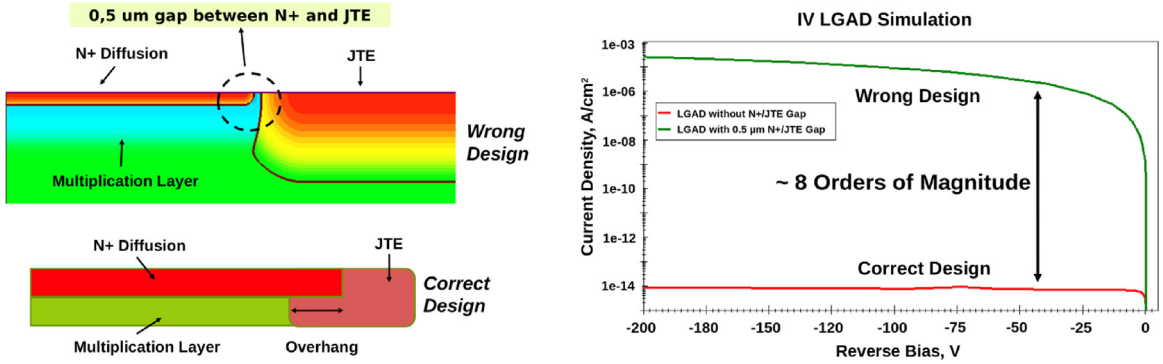

Fig. 6. 2D Numerical simulation at the pad peripheral area of the LGAD. The gap between N^+ and JTE diffusion was found to reproduce the high leakage current problem experimentally observed. The problem was mitigated by introducing an overhang of the N^+ into the JTE diffusion.

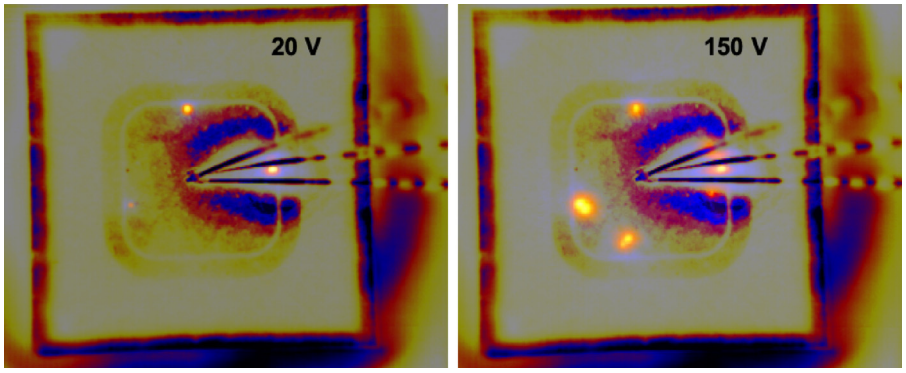

Fig. 7. Thermographic image of one LGAD biased at 20 and 150 V. Several points of high current generation can be observed at its periphery, increasing its number and intensity as the voltage applied to the LGAD increases.

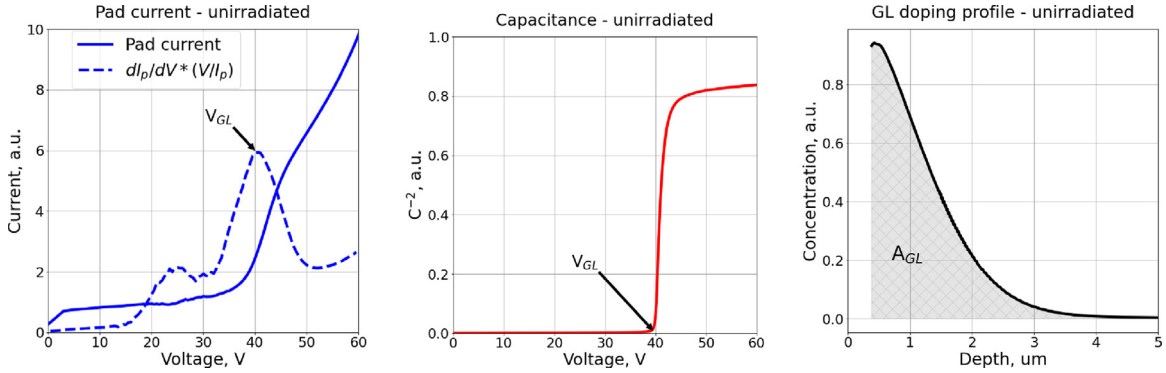

Fig. 8. In the left: extraction of the V_{GL} from the pad current curve. In the center: extraction of the V_{GL} from the capacitance curve. In the right: calculation of the total active B present in the GL (A_{GL}) by integrating over the doping profile extracted from the CV curves.

CV curves, the V_{GL} is identified at the point in which the capacitance curve drops due to the depletion of the bulk, which can be identified in the C^{-2} plot as indicated in Fig. 8 middle. The last method uses the GL doping profile extracted from the CV curves using Eq. (2), where C is the capacitance and A the area of the sensor, q the elementary charge, ϵ_0 the permittivity of vacuum and ϵ_r the relative permittivity of silicon. By integration over the profile, we can get the total active B concentration of the GL (A_{GL}). This is shown in Fig. 8 right.

$$N_x(x) = \frac{C^3}{q\epsilon_0\epsilon_r A^2 dC/dV} \quad \text{with} \quad x = \frac{\epsilon_0\epsilon_r A}{C} \tag{2}$$

Following these three methods, the acceptor removal coefficient (c_n) for the neutron-irradiated samples was extracted. This is shown in Fig. 9. From the IV and CV data, where V_{GL} is extracted, the c_n is very similar, but from the GL doping profile method, the c_n that we get is slightly smaller.

6. Radiation tolerance of the LGAD gain

The gain studies were done with the IR-laser (1060 nm) and Sr-90 source setups of the SSD lab at CERN. The setups and the measurement conditions are well described in this paper [16]. Specifically, the gain of the samples from run 11748 was evaluated using the IR-laser setup and the gain of the samples from run 12916 using the Sr-90 source setup. The reason for this was the unavailability of the Sr-90 source during the campaign of measurements with run 11748. For these measurements, the sensors were glued on a passive PCB and read out using a cividec C2 current amplifier (2 GHz, 40 dB). After the amplification stage, the signal was digitized with an Agilent DSO 9254 Oscilloscope (2.5 GHz, 20 Gsa/s).

For the laser measurements, the intensity of the IR-laser was tuned to generate an equivalent charge of ~15 MIPs with a beam laser spot

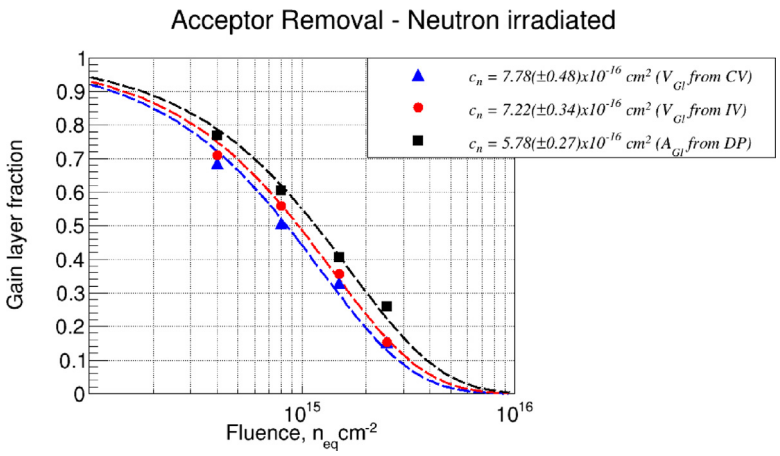

Fig. 9. Acceptor removal parameterization using the three methods described in this paper for the neutron-irradiated LGADs.

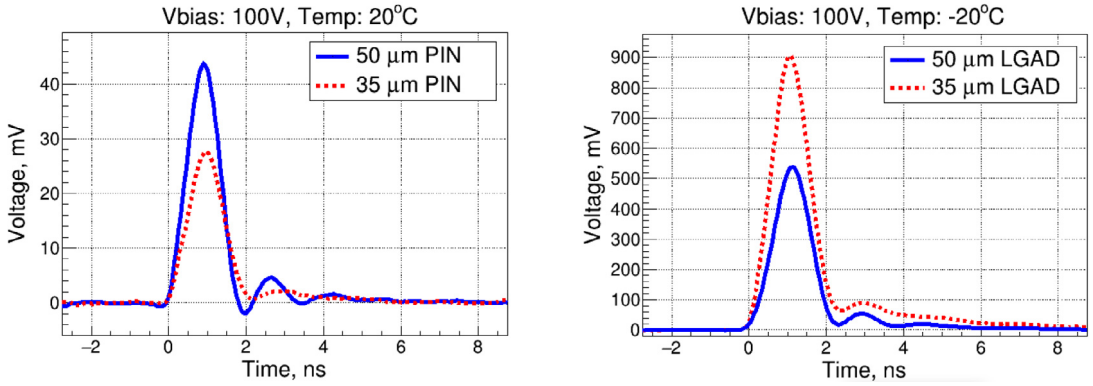

(a) TCT PIN's waveforms (b) TCT LGAD's waveforms

Fig. 10. Examples of TCT pulses taken with two unirradiated PIN diodes and two unirradiated LGADs from both wafers of run 11748. The charge collected was computed as the integral of the pulses within a time window of 6 ns.

size of around 20 µm in FWHM. To correct possible fluctuations of the laser intensity during the measurements, an independent reference sensor is used to normalize the data to the laser power. To improve the SNR, a waveform averaging of 256 was used on the oscilloscope. The measurements were performed at −20 °C with the guard ring left floating. As a reference, in Fig. 10(a) two TCT pulses recorded for a PIN diode from each wafer at 100 V are shown. The difference in amplitude is due to the difference in active thickness (∼30%). In Fig. 10(b) two TCT pulses for two unirradiated LGAD samples from each wafer are shown. Despite the fact that the bias voltage is the same in both cases (100 V), the pulse amplitude of the 35 µm LGADs is higher than the pulse amplitude of the 50 µm. This is because at the same voltage, in the thinner LGAD, the electric field is higher, and in consequence, the impact ionization process is magnified. In other words, the gain at 100 V for the 35 µm LGAD is higher as expected.

The Sr-90 measurements were performed under the same conditions: −20 °C, and the guard ring was left floating. Three samples were measured at the same time in a 3-sensors stack configuration, where the bottom one was always the reference. In order to measure the gain, the charge collected in a PIN diode was measured using a charge-sensitive amplifier, obtaining a Most Probable Malue (MPV) in the Landau distribution of 0.50 fC. This is in agreement with the expected value for a 50 µm thick sensor.

In both cases, IR-laser and Sr-90 source, the gain was evaluated as the ratio between the LGAD collected charge ($CC_{LGAD}[V]$) and the unirradiated PIN collected charge after full depletion ($CC_{PIN}[V \geq V_{FD}]$), from the same wafer, as a function of the reverse bias voltage (V) as expressed by:

$$Gain[V] = \frac{CC_{LGAD}[V]}{CC_{PIN}[V \geq V_{FD}]} \tag{3}$$

For the Sr-90 source measurements, the charge was derived from the MPV of the Landau distribution, and for the IR-laser from the mean value of the Gaussian distribution. To estimate the collected charge for a MIP we should multiply the gain by ∼0.35 fC and ∼0.5 fC for the 35 µm and 50 µm thin LGADs respectively. Notice that we have chosen to be conservative with the maximum operating voltages for the case of the proton-irradiated LGADs. At the time of these measurements, the limit of 11−12 V/µm to avoid fatal breakdown was not well established, so, preventively, we decided to operate the LGADs at biasing voltages below 450 V (550V) for 35 µm (50 µm) thick LGADs to avoid fatal breakdowns [17,18]. Because of the gain reduction mechanism present in LGADs [16], they are expected to show slightly less gain when they are measured with the IR-laser set to an intensity of ∼15 MIPs with a beam spot of ∼20 µm in FWHM, than when they are measured with the Sr-90 source, generating only 1 MIP (but also over a much narrower ionizing path). This effect is especially relevant at high values of the gain therefore, we do not expect a significant difference in the case of the irradiated LGADs and only a reduction of about 5%–10% in the case of the unirradiated ones at gains greater than 20 [19].

A comparison between the charge collected between the PINs as a function of the voltage with the IR-laser is shown in Fig. 11(a). In both cases, the depletion voltage is below 5 V and after the full depletion, the charge collected is constant. The charge, shown in arbitrary units, scales with the thickness; the 35 µm PIN collects 30% less charge as the

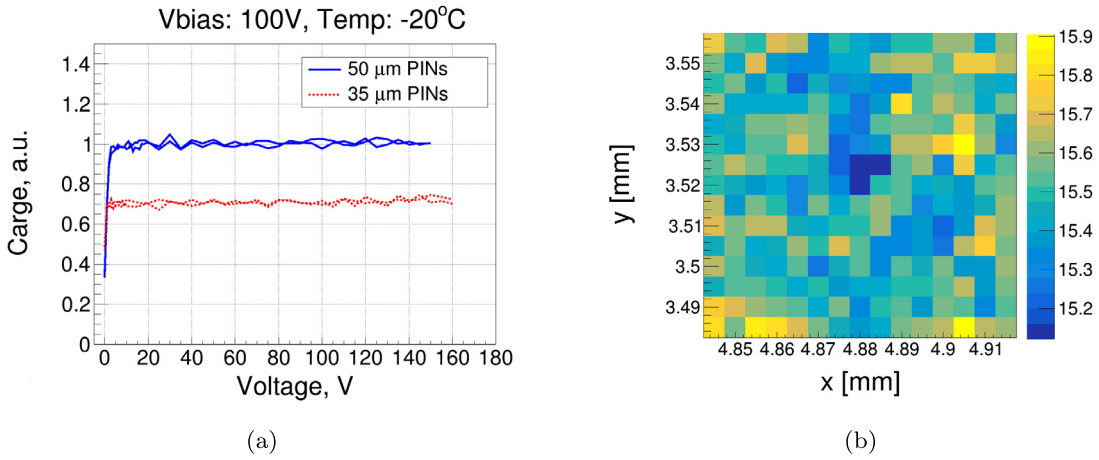

Fig. 11. (a) Comparison between PINs charge collection from wafers W5 and W11. (b) Gain surface homogeneity in one of the unirradiated LGADs from wafer W11.

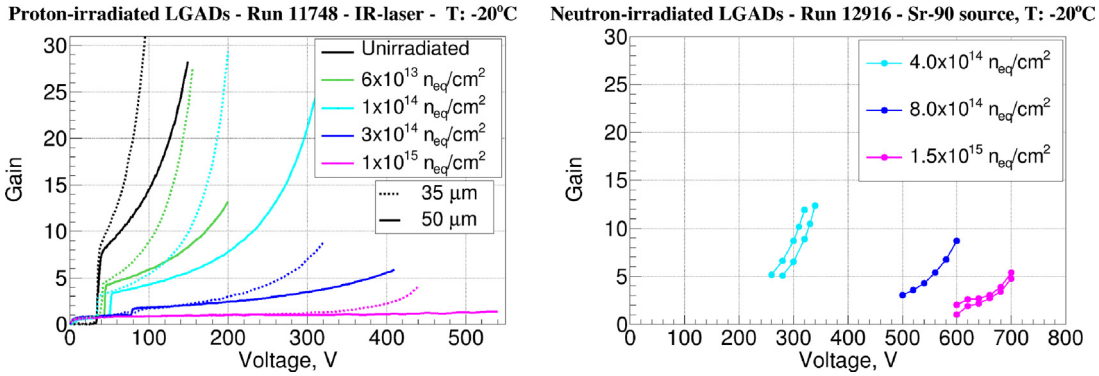

Fig. 12. Gain measurements after irradiation. The gain was evaluated according to the expression (3). A gain degradation with fluence is observed (more severe in the case of protons) and a higher gain degradation of the 50 µm LGADs with respect to the 35 µm ones can be seen.

difference in thickness was anticipating. Also, the gain homogeneity along the surface of the LGADs was measured. An XY scan was done within the 100×100 µm^2 metallization opening. In Fig. 11(b), as an example, the XY gain scan at 100 V for a 50 µm thick unirradiated LGAD is plotted. The gain variation measured on the metallization opening was less than 3% in all the samples.

Fig. 12 reports on the gain measured before and after irradiation as a function of the reverse bias voltage. Before irradiation the 50 µm LGADs from run 11748 present a gain that ranges from 8 to 30 in the range of voltages measured. In the case of the 35 µm LGADs, the gain ranges from 10 to 32 in a more narrow voltage range. As mentioned before, this is because in the thinner devices there is a higher electric field for the same voltage, which implies a higher drift velocity and a magnification of the impact ionization process. For the 50 µm LGADs from run 12916, the gain is much higher and ranges from 60 to 100 in a very narrow range of voltages, as the breakdown voltage at −20 °C is below 60 V.

A gain degradation with fluence is reported for all LGADs. Although by increasing the reverse bias voltage it is possible to recover part of the lost gain, in the case of the proton irradiated LGADs for a fluence of 1×10^{15} n_{eq}/cm^2 the gain degradation is very severe, especially for the 50 µm LGADs, and the gain cannot be recovered in the studied voltage range. For the neutron-irradiated LGADs this is happening for a fluence of 2.5×10^{15} n_{eq}/cm^2. In the case of the proton irradiated LGADs, the gain in the 50 µm LGADs is more degraded than in the 35 µm ones, as reflected in the observation that lower maximum gain values were reached at highest operation voltages. This means that assuming the same degradation in the amplification layer, the thicker substrate is responsible for the stronger decrease in collected charge. This is related to a higher drop of potential over the thicker bulk, a lower fraction of the overall generated electrons arriving at the gain layer, and a higher fraction of the holes resulting from the amplification process not reaching the back electrode, respectively traversing a lower fraction of the overall bulk thickness. The results for the highest fluences of 3×10^{15} n_{eq}/cm^2 for protons and 2.5×10^{15} n_{eq}/cm^2 for neutrons, are not reported as too much degradation in the gain was observed after 1×10^{15} n_{eq}/cm^2 and 1.5×10^{15} n_{eq}/cm^2 respectively.

Another interesting observation is that the V_{GL} is increasing with the fluence in the case of the proton irradiated LGADs from run 11748. This result goes in the same line as the capacitance measurements and confirms that the acceptor removal effect cannot be extracted from the V_{GL}. Thus, based on these results, the radiation damage effect that is dominating the shape of the CV curve has to be the double junction effect [14] enhanced by the large leakage current.

7. Timing study with laser

7.1. Jitter evaluation: Slew rate and noise measurements

An evaluation of the jitter obtained from the slew rate (SR) of the pulses and the baseline noise from the TCT measurements with IR laser, on LGADs from run 11748, is presented here. For the jitter estimation, the same conditions were maintained in the setup as for the TCT measurements presented in the last section.

The SR can be computed as the ratio between the amplitude of the pulse (A) and the rise time (RT), but this represents a calculation of an average SR of the pulse. Therefore, for a more precise evaluation of the jitter, the highest SR was taken for every pulse (P(t)). This was done by obtaining the maximum in the derivative of the pulse,

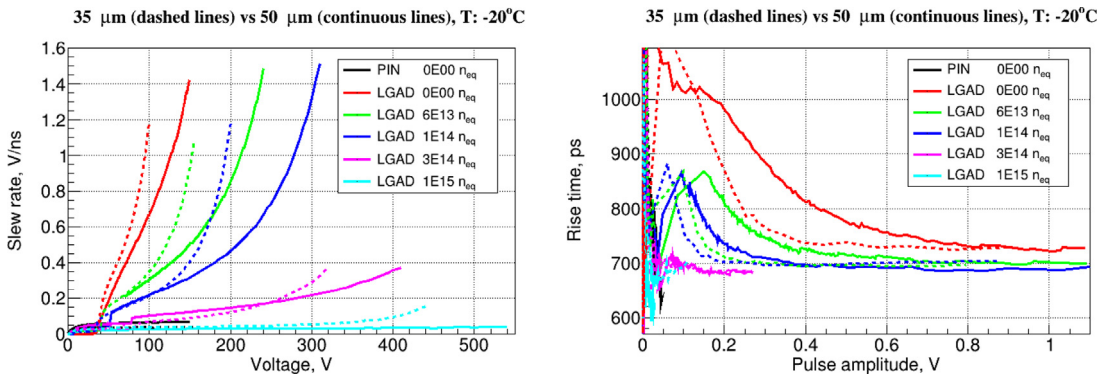

Fig. 13. On the left side: SR values as a function of the voltage for all the samples. Like with the gain, the SR degrades with fluence and the 35 µm LGADs are less affected in comparison with the 50 µm ones. On the right side: $RT_{(10/90)}$ measured as a function of the pulse amplitude. The RT reaches a stable value of ∼720 ps for all the devices.

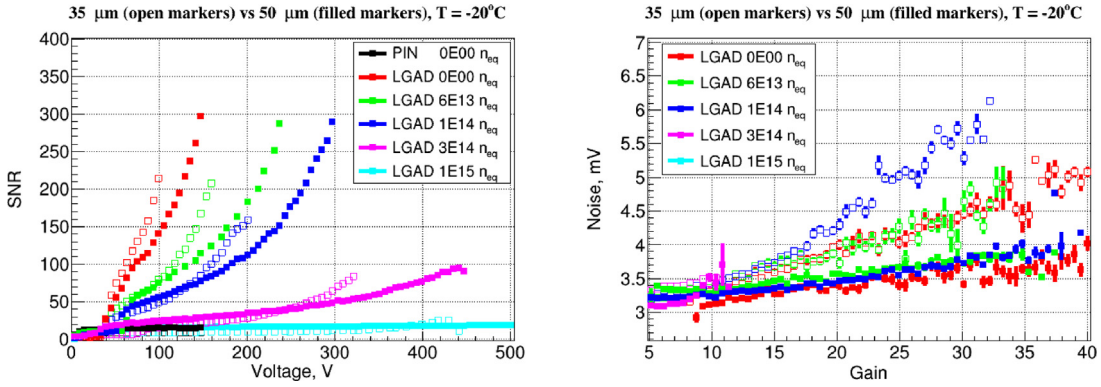

Fig. 14. On the left side: Signal-to-noise ratio (SNR) values as a function of the voltage for all the samples. The SNR degrades with fluence and the 35 µm LGADs are less affected in comparison with the 50 µm LGADs. On the right side: Noise measured as a function of the gain for all the LGADs. It can be observed that the noise increases linearly with the gain.

which generally appeared around the 50% of the pulse amplitude and is described by Eq. (4):

$$SR_{max} = \left(\frac{dP(t)}{dt}\right)_{max} \tag{4}$$

In Fig. 13 left, the SR results using formula (4) are shown. These results correspond to a laser intensity equivalent to ∼15 MIPs. The SR value measured for the PIN diodes at 100 V was: 0.065 V/ns for the 50 µm PIN and 0.040 V/ns for the 35 µm one. For the unirradiated LGADs, the SR value increases with the gain and after irradiation, a degradation with increasing fluence is observed.

Considering the obtained SR values, a good timing performance of the LGADs up to a fluence of $3\times10^{14}\ n_{eq}/\text{cm}^2$ is expected. Generally, the thinner LGADs show better behavior compared with the thicker ones when both are operated at the same bias voltage. Already at a fluence of $1\times10^{15}\ n_{eq}/\text{cm}^2$ the SR drops to a value of ∼0.16 V/ns at the highest measured voltage for the 35 µm LGADs while in the 50 µm LGADs, the SR reaches only a value of ∼0.04 V/ns; the latter value is already lower than the value measured for the PIN diode at 100 V. Also, in Fig. 13 right side the $RT_{(10/90)}$, time taken by the pulse to change from 10% to 90% of its amplitude, is shown as a function of the pulse amplitude. The RT for a sufficiently high pulse amplitude reaches a plateau at around 720 ps. Thus, we can consider this a good estimator of the RT at the optimum working point for these devices.

The SNR was evaluated as the ratio between the pulse amplitude and the noise. The noise (δ_{noise}) was calculated as the RMS of the baseline during the first 8 ns of the waveform. For the noise measurements, only one waveform per measurement was recorded. This allows us to measure the baseline noise and evaluate the correct SNR. The results are reported in Fig. 14 left. Unirradiated LGADs present a good SNR, and for the same bias voltage, it is better for the thinner ones as expected; and degradation is observed with fluence. The SNR measured for the PIN diodes at 100 V was: 15 for the 50 µm PIN and 10 for the 35 µm one. The degradation of the SNR at a fluence of $1\times10^{15}\ n_{eq}/\text{cm}^2$ brings this value close to the PIN samples, being 30 the maximum SNR for the 35 µm LGAD at ∼420 V and 20 for the 50 µm LGAD at ∼500 V.

Another important parameter is the noise as function of voltage, which has been evaluated for all the samples. This is reported in Fig. 15. At low voltages, the noise level is the same for both thicknesses and it is dominated by the electronics. In fact, this ∼3.2 mV is the baseline noise present in the experimental setup. This implies that the onset voltage where the noise starts to increase is hidden in the plots. Nevertheless, it can be observed that the noise increases exponentially after a certain voltage and this increase is related to the gain present in each device. That is why in the 35 µm LGADs the noise increases more rapidly than in the 50 µm LGADs. To visualize the relation between noise and gain, the noise as a function of the gain was plotted in Fig. 14 right side. It is shown that the noise increases linearly with the gain above the baseline noise of the system (∼3.2 mV). The increase of the noise is higher for the 35 µm LGADs, where for the unirradiated and the one irradiated to $6\times10^{13}\ n_{eq}/\text{cm}^2$, the increase for the gain unit is 0.05 mV, being 0.12 mV for the ones irradiated at $1\times10^{14}\ n_{eq}/\text{cm}^2$. Meanwhile, for the 50 µm LGADs, the noise increases only between 0.02 and 0.025 mV per unit of gain in the same cases.

Finally, the jitter (δ_{time}) can be extracted following the approximation given by Eq. (5) as a function of the δ_{noise} and the SR_{max}. Also, on Eq. (6) is calculated the δ_{time} as a function of the rise time (RT) and SNR. It is possible to replace $RT_{(10/90)}$ for the measured value of ∼ 720 ps, linking directly the (δ_{time}) and the SNR.

$$\delta_{time} \equiv \frac{\delta_{noise}}{|\frac{\delta V}{\delta t}|} \equiv \frac{\Delta t}{\Delta V} \times \delta_{noise} = \frac{\delta_{noise}}{SR_{max}} \tag{5}$$

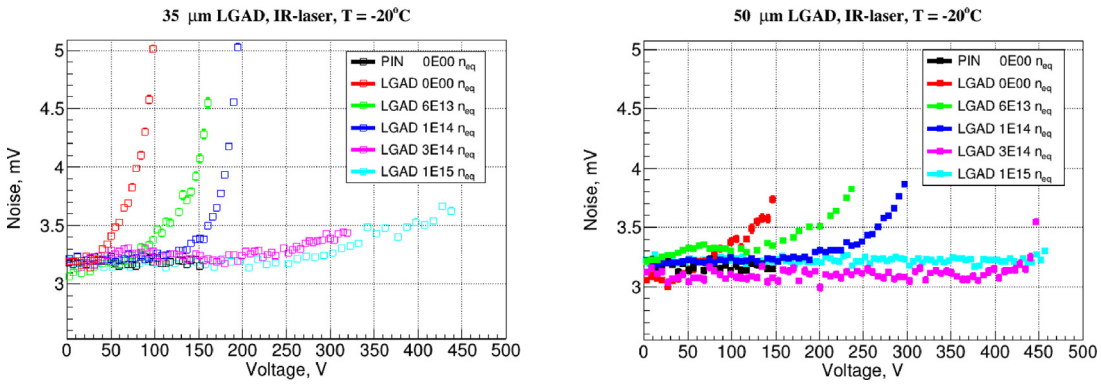

Fig. 15. Noise comparison between proton irradiated LGADs from the two wafers from run 11748. On the left side 35 μm LGADs, and on the right side 50 μm LGADs.

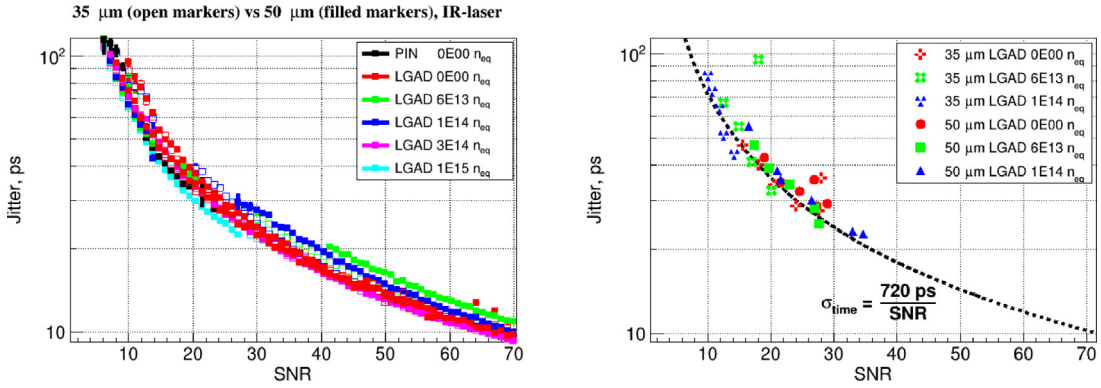

Fig. 16. On the left: jitter as a function of the SNR calculated according to expression (5). On the right: jitter measured using the IR-laser timing setup described in Fig. 17 on the proton irradiated LGADs from run 11748. The dotted line represents the reference values from expression (6).

$$\delta_{time} \equiv \frac{\Delta t}{\Delta V} \times \delta_{noise} = \frac{\Delta t}{\frac{\Delta V}{\delta_{noise}}} \approx \frac{RT}{SNR} = \frac{720\,ps}{SNR} \tag{6}$$

In Fig. 16 left, the δ_{time} calculated as a function of the SNR for all the samples is shown. All sensors follow the same trend as indicated by Eq. (6). The jitter contribution depends only on the SNR as far as the pulse shape does not change with gain or radiation as in the present case. PINs and LGADs are on the same line, even irradiated LGADs follow the same trend and no distinctions are visible between the sensors of different thicknesses. This result shows that as long as the SNR can be maintained, the jitter does not change. It is important to stress that the jitter partially estimates the timing resolution, the contribution from the non-uniform ionization along the particle's track, the so-called *Landau fluctuation* contribution, is not present in a laser-based setup. Anyhow, the increase of the jitter induced by the radiation is similar to the expected degradation of the timing performance with the fluence since no significant change of the leading edge of the pulses, other than the amplitude, has been observed in the irradiated samples.

7.2. Timing performance

The time resolution with IR laser was measured for some of the devices to cross-check the previous approximations and to get a more realistic value. The measurements were carried out in the same set-up but slightly modified to perform dedicated timing measurements. The main idea was to avoid any external time reference in order to reduce the uncertainty in the measurements coming from its intrinsic time resolution. The schematic of the set-up is shown in Fig. 17. Each IR laser pulse is split into two lines with each carrying half of the intensity. In one line a fixed delay of ~50 ns is introduced. Then, these two lines are recombined in one line again which illuminates the Device Under Test (DUT). In this way, a fixed time interval between laser pulses arriving at the DUT is introduced and the use of an external reference is not needed. The difference in intensity between the two pulses was about 1.5%. For these measurements, the IR laser intensity was reduced to an equivalent intensity of ~1 MIP (per pulse), the internal waveform averaging on the oscilloscope was removed, and 2000 single events were collected per measurement.

In order to estimate the jitter, a constant fraction discriminator (CFD) algorithm was used. The two pulses, present in a single waveform, were studied independently, though no differences were observed between them. In this way, different CFD thresholds were applied to find the best threshold combination that gives the best time resolution between the two pulses. The time resolution is extracted as the width of the distribution of time differences, divided by the square root of 2. The bias voltage chosen for each LGADs was the one that maximizes the SNR and in consequence, minimizes the jitter. In Table 3 the measured jitter for each LGAD along with the bias voltage, SNR, gain, noise level, and the $RT_{(10/90)}$ at the optimal point (highest SNR) are summarized. For this part of the study, only the unirradiated LGADs and the ones irradiated at the two lowest fluences were considered. Looking at the parameters in the table, one can conclude that the 50 μm LGADs perform better than the 35 μm ones. They are able to achieve a higher SNR and in consequence a lower jitter. The gain, at this working point, is much higher for the thicker LGADs.

In Fig. 16 right, the obtained jitter as a function of the SNR is shown. Some more points at different bias voltages were taken per sensor close to the optimal point. The approximation obtained in the previous section, Eq. (6), is plotted as a reference. It is shown that the measured points follow the trend indicated by this approximation and both results, timing measurements and jitter evaluation, are consistent. The timing jitter measurement for the case that the SNR is less than the optimal value also follows the predicted curve.

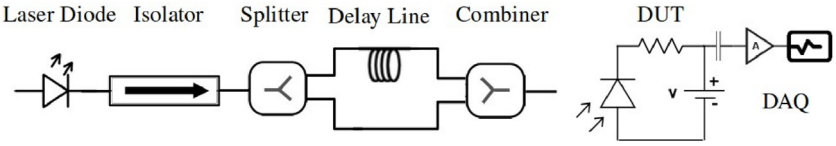

Fig. 17. Timing setup schematic with all its main components: laser diode, isolator, splitter, delay line, combiner, and DUT.

Table 3
Table summarizing the best jitter measurements achieved with the IR-laser timing setup along with experimental parameters.

Thickness	Fluence	Jitter (ps)	SNR	Vbias (V)	Gain	Noise (mV)	RT (ps)
35 μm	unirradiated	27.5	27.7	120	141	13	690
35 μm	$6 \times 10^{13}\ n_{eq}/\mathrm{cm}^2$	32.5	20.1	165	64	4.8	673
35 μm	$1 \times 10^{14}\ n_{eq}/\mathrm{cm}^2$	43.5	14.2	200	54	5.8	676
50 μm	unirradiated	28.6	27.3	175	86	6.8	660
50 μm	$6 \times 10^{13}\ n_{eq}/\mathrm{cm}^2$	24.7	27.7	280	81	6.3	667
50 μm	$1 \times 10^{14}\ n_{eq}/\mathrm{cm}^2$	22.7	35.1	320	118	6.7	633

It is clear that the lowest jitter will be found at the highest SNR reachable with each sensor. It is needed to understand what is degrading the SNR after this working point. This will define the maximum operating bias voltage for each sensor, as it should work in stable conditions and at its best timing performance. Trying to increase the bias voltage after this optimal point will lead to an underperforming configuration and means entering a very high noise regime that will degrade the jitter dramatically.

For a better understanding of the performance of these LGAD sensors, a finer voltage scan was done for one of the 50 μm LGADs irradiated at $1 \times 10^{14}\ n_{eq}/\mathrm{cm}^2$. The scan was done at three different temperatures: −20 °C, −15 °C, −10 °C, around the optimal bias voltage (∼320 V). The measured SNR as a function of the bias voltage is shown in Fig. 18 on the left side. In this plot, it is shown that the highest SNR achieved was ∼35, which means that the best jitter is ∼22.7 ps independently of the temperature. The main impact of temperature is that the bias voltage at which the highest SNR is reached slightly increases with rising temperature. Also, the range in voltages at which the SNR stays above a certain threshold is wider at a higher temperature. In plot 18 on the right side, some waveforms at two bias voltages: 320 V and 334 V, are shown for each investigated temperature. At 320 V, the gain at −20 °C is much higher than the gain at −10 °C, which implies that the sensor reaches its maximum SNR at lower voltages. However, at 334 V, despite the fact that at −20 °C the gain is higher, the presence of a higher noise is degrading the SNR rapidly, as the amplitude and the number of randomly appearing noise spikes is increasing and amplified as well. At −20 °C the noise spikes start to become comparable to the signal, making it impossible to get proper data any longer. At 320 V, the higher noise observed at −20 °C is not yet relevant and the sensor still performs well. The appearance of this high noise in the sensors clearly delimits their working voltage range and their timing performance. The bias voltages given in Table 3 minimize the jitter and delimit the voltage range.

8. Timing study with beta source

Timing measurements were performed with a Sr-90 source on the neutron-irradiated LGADs from run 12916. The measurement conditions were the same as the ones described for the gain measurements in the previous section. All samples were measured at −20 °C and the guard ring was left floating. One unirradiated LGAD was used as a reference and presented a time resolution of ∼30 ps. With the 3-sensor stack configuration, two LGADs were measured at the same time, while the third sensor in the stack was the reference LGAD. For the time resolution evaluation, the constant fraction discrimination (CFD) method was used.

The charge and the time resolution obtained with the Sr-90 source for all the neutron-irradiated LGADs are shown in Fig. 19. In these plots, the results for the unirradiated LGADs are not included. They presented a charge above 15 fC with a time resolution of ∼30 ps at −20 °C, which was within the expected value range. In the case of the irradiated LGADs, a clear degradation in the charge and time resolution with fluence is reported. Taking into consideration the requirements posed by the LHC phase II upgrade experiments, a time resolution below 50–70 ps for a maximum bias voltage of 600V [20], is only achieved for the fluences of $4 \times 10^{14}\ n_{eq}/\mathrm{cm}^2$ and $8 \times 10^{14}\ n_{eq}/\mathrm{cm}^2$. For the fluence of $1.5 \times 10^{15}\ n_{eq}/\mathrm{cm}^2$ the degradation in the time resolution is more severe and below 600 V, the time resolution is above 80 ps. Results for the highest fluence ($2.5 \times 10^{15}\ n_{eq}/\mathrm{cm}^2$) are not included because the SNR was too small for a proper estimation of the time resolution.

9. Conclusions

The radiation tolerance of IMB-CNM LGADs based on a shallow and broad multiplication layer is studied in this paper. LGADs from two different production runs (11748 and 12916) were used: the LGADs from run 11748 were irradiated with protons at CERN-PS up to a fluence of $3 \times 10^{15}\ n_{eq}/\mathrm{cm}^2$, and the LGADs from run 12916 were irradiated with neutrons at JSI in Ljubljana up to a fluence of $2.5 \times 10^{15}\ n_{eq}/\mathrm{cm}^2$. The LGAD manufacturing run 11748 includes sensors with an active thickness of 35 μm in addition to the baseline active thickness of 50 μm.

The electrical characterization of the run 11748 LGADs revealed a design problem that caused a very high leakage current in all the LGAD samples. The origin of the problem was found, and its correction resulted in the production run 12916, which yielded low leakage current LGAD sensors. Despite the leakage current problem of run 11748, it was possible to complete the radiation tolerance study of these sensors too.

Using an IR-laser setup, the gain and timing performance was evaluated before and after proton irradiation of LGADs from run 11748. In terms of gain, a better behavior of the 35 μm thick LGADs was observed; they present a more moderate gain degradation after irradiation and a potentially better timing performance with a higher slew rate. Nevertheless, due to the faster increase of the noise in the 35 μm LGADs with the bias voltage, the maximum signal-to-noise ratio (SNR) achieved in these samples is lower compared with the 50 μm thick LGADs; therefore, a better jitter was found for the 50 μm thick LGADs. The sudden increase of noise with the bias voltage in all investigated samples could be caused by the higher electric field present in the thinner devices, making them more prone to microdischarges.

Using a Sr-90 source setup, the gain and time resolution were evaluated, before and after neutron irradiation, in LGADs from run 12916. As expected, a degradation of the gain and time resolution with fluence was observed. A timing performance suitable for the requirements of the future timing layers of the CMS and ATLAS experiments was achieved up to a fluence of $8 \times 10^{14} n_{eq}/\mathrm{cms}^2$. The time resolution

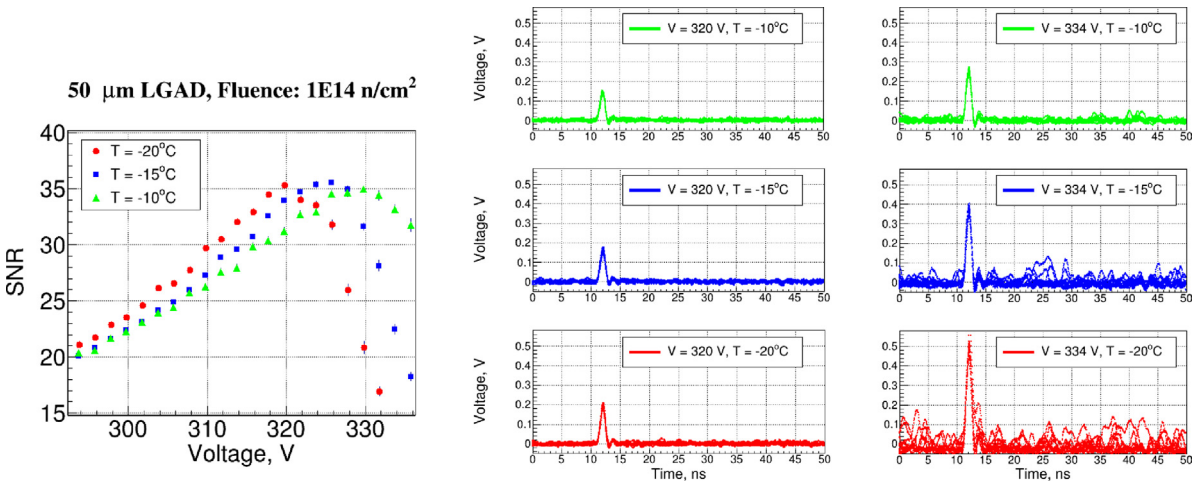

Fig. 18. SNR as a function of the bias voltage at three different temperatures: −20 °C, −15 °C and −10 °C; and TCT waveforms at two different bias voltages: 320 V and 334 V for each temperature. Data from a 50 μm proton-irradiated LGAD from run 11748.

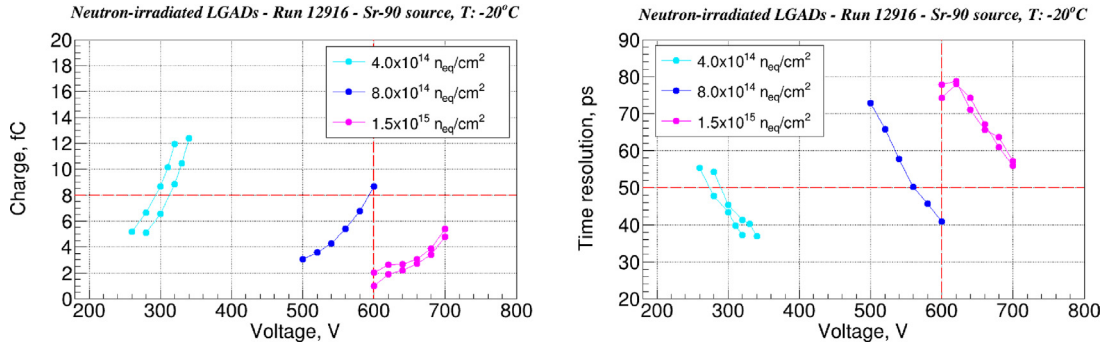

Fig. 19. Charge and time resolution for the neutron-irradiated LGADs measured with a Sr-90 source. A clear degradation of both parameters with fluence is observed. The horizontal dashed lines represent the requirements from the CMS-ETL detector: charge >8 fC and time resolution <50 ps. Also, the maximum operational bias voltage of 600 V is highlighted in both plots.

achieved for an end-of-life fluence of $1.5\times10^{15} n_{eq}/\mathrm{cm}^2$ and a maximum operating voltage of about 600 V, to prevent the radiation-induced fatal breakdown of the LGAD sensors, is of 80 ps. This can be improved by carbon co-implantation in the gain layer [21]. A recent production run at IMB-CNM of carbonated LGADs (run 15246) is currently under study and is expected to significantly improve the radiation tolerance of the LGADs based on a shallow and broad multiplication layer design.

Declaration of competing interest

The authors declare that they have no known competing financial interests or personal relationships that could have appeared to influence the work reported in this paper.

Data availability

Data will be made available on request

Acknowledgments

This work was developed in the framework of the RD-50 collaboration and has been supported by the Spanish Ministry of Science and Innovation (MCIN/AEI/10.13039/501100011033/), by the European Union's ERDF program "A way of making Europe" (Grant References PID2020-113705RB-C31, PID2020-113705RB-C32, and PID2021-124660OB-C22) and by the European Union's Horizon 2020 Research and Innovation funding program, under Grant Agreement no. 101004761 (AIDAInnova). We thank Dr. Miquel Vellvehi and Dr. Xavier Perpiña (IMB-CNM-CSIC) for their work in performing the thermographic measurements.

References

[1] High-Luminosity Large Hadron Collider (HL-LHC): Technical Design Report, in: CERN Yellow Reports: Monographs, CERN, Geneva, 2020, http://dx.doi.org/10.23731/CYRM-2020-0010, URL https://cds.cern.ch/record/2749422.

[2] Technical Proposal for a MIP Timing Detector in the CMS Experiment Phase 2 Upgrade, Tech. Rep. CERN-LHCC-2017-027. LHCC-P-009, CERN, Geneva, 2017, URL https://cds.cern.ch/record/2296612.

[3] Technical Proposal: A High-Granularity Timing Detector for the ATLAS Phase-II Upgrade, Tech. Rep. CERN-LHCC-2018-023. LHCC-P-012, CERN, Geneva, 2018, URL https://cds.cern.ch/record/2623663.

[4] G. Pellegrini, et al., Technology developments and first measurements of low gain avalanche detectors (LGAD) for high energy physics applications, Nucl. Instrum. Methods Phys. Res. A 765 (2014) 12–16, URL http://www.sciencedirect.com/science/article/pii/S0168900214007128.

[5] N. Cartiglia, et al., Design optimization of ultra-fast silicon detectors, Nucl. Instrum. Methods Phys. Res. A 796 (2015) 141–148, URL http://www.sciencedirect.com/science/article/pii/S0168900215004982.

[6] M. Mandurrino, Silicon Detectors for the LHC Phase-II Upgrade and Beyond, RD50 Status Report, 2019, URL https://arxiv.org/abs/1910.06045.

[7] E. Currás, Low Gain Avalanche Detectors for 4-dimensional tracking applications in severe radiation environments, JPS Conf. Proc. 34 (2021) 010015, URL https://journals.jps.jp/doi/abs/10.7566/JPSCP.34.010015.

[8] M. Moll, Acceptor removal - Displacement damage effects involving the shallow acceptor doping of p-type silicon devices, Proc. Sci. (2019) URL https://pos.sissa.it/373/027/pdf.

[9] B. Gkotse, M. Glaser, M. Moll, F. Ravotti, IRRAD: The new 24 GeV/c proton irradiation facility at CERN, in: 12th International Topical Meeting on Nuclear Applications of Accelerators, 2015, pp. 182–187, URL https://inspirehep.net/files/2d9bebc69cf808a7021e5a9aec714e97.

[10] P. Allport, F. Bögelspacher, K. Bruce, R. Canavan, A. Dierlamm, L. Gonella, P. Knights, I. Mateu, M. Moll, K. Nikolopoulos, B. Phoenix, T. Price, L. Ram, F. Ravotti, C. Simpson-Allsop, C. Wood, Experimental determination of proton

hardness factors at several irradiation facilities, J. Instrum. 14 (12) (2019) P12004, http://dx.doi.org/10.1088/1748-0221/14/12/P12004.

[11] D. Žontar, V. Cindro, G. Kramberger, M. Mikuž, Time development and flux dependence of neutron-irradiation induced defects in silicon pad detectors, Nucl. Instrum. Methods Phys. Res. A 426 (1) (1999) 51–55, http://dx.doi.org/10.1016/S0168-9002(98)01468-5.

[12] D. Campbell, A. Chilingarov, T. Sloan, Frequency and temperature dependence of the depletion voltage from CV measurements for irradiated Si detectors, Nucl. Instrum. Methods Phys. Res. A 492 (3) (2002) 402–410, URL https://www.sciencedirect.com/science/article/pii/S0168900202013530.

[13] A. Himmerlich, N. Castello-Mor, E. Currás-Rivera, Y. Gurimskaya, V. Maulerova-Subert, M. Moll, I. Pintilie, E. Fretwurst, C. Liao, J. Schwandt, Defect characterization studies on irradiated boron-doped silicon pad diodes and low gain avalanche detectors, Nucl. Instrum. Methods Phys. Res. A 1048 (2023) 167977, URL https://www.sciencedirect.com/science/article/pii/S0168900222012694.

[14] S. Ugobono, et al., Multiplication onset and electric field properties of proton irradiated LGADs, Proc. Sci. (2018) 041, http://dx.doi.org/10.22323/1.309.0041.

[15] G. Kramberger, et al., Radiation effects in low gain avalanche detectors after hadron irradiations, J. Instrum. 10 (07) (2015) P07006, http://dx.doi.org/10.1088/1748-0221/10/07/P07006.

[16] E. Currás, M. Fernández, M. Moll, Gain reduction mechanism observed in low gain avalanche diodes, Nucl. Instrum. Methods Phys. Res. A (2022) 166530, URL https://www.sciencedirect.com/science/article/pii/S0168900222001371.

[17] R.J. Lipton, LGAD Single Event Burnout Studies, Report Number: FERMILAB-FN-1141-CMS (2021), 2021, URL https://www.osti.gov/biblio/1841397.

[18] G. Laštovička-Medin, et al., Studies of LGAD performance limitations, single event burnout and gain suppression, with femtosecond-laser and ion beams, Nucl. Instrum. Methods Phys. Res. A 1041 (2022) 167388, URL https://www.sciencedirect.com/science/article/pii/S0168900222006921.

[19] E. Currás, et al., Gain suppression mechanism observed in low gain avalanche detectors, in: The 38th RD50 Workshop at CERN, Geneva, 2021, URL https://indico.cern.ch/event/1029124/contributions/4411287/.

[20] M. Wu, A High-Granularity Timing Detector for the ATLAS Phase-II Upgrade, Tech. Rep., CERN, Geneva, 2023, URL https://cds.cern.ch/record/2846406.

[21] S.M. Mazza, et al., Tuning of gain layer doping concentration and carbon implantation effect on deep gain layer, J. Phys. Conf. Ser. 2374 (1) (2022) 012173, http://dx.doi.org/10.1088/1742-6596/2374/1/012173.